

# An Improved Apparatus For Measuring the Growth of Ice Crystals from Water Vapor

Kenneth G. Libbrecht

Department of Physics, California Institute of Technology  
Pasadena, California 91125

**Abstract.** We describe an apparatus designed for obtaining precise measurements of the growth rates of ice crystals from water vapor over a range of experimental conditions. Our aim is to produce clean, high-quality test crystals in a well controlled environment for investigating the detailed molecular dynamics that controls the basic physics of ice crystal growth. In this paper we describe the nucleation and initial growth of test crystals, their transport and selection into a experimental chamber, the creation of a stable and controllable supersaturation, hardware and calibration issues, and the crystal measurement via direct imaging and broad-band interferometry.

[Note: The figures in this paper are presented at reduced resolution to facilitate rapid downloading. The paper is available with higher quality figures at <http://www.its.caltech.edu/atomic/publist/kglpub.htm>, or by contacting the author.]

## 1 Investigating the Physics of Ice Crystal Growth

The goal of our ice growth experiments is to observe the growth of individual ice crystals in a carefully controlled environment, and an idealized schematic diagram of our experimental set-up is shown in Figure 1. The top surface of the chamber is a thermal conductor with a uniform temperature  $T_{IR}$ , and its inside surface is covered with a layer of ice crystals that make up the ice reservoir. At the beginning of each measurement a single test crystal is positioned near the center of the bottom substrate surface held at temperature  $T_{subst}$ , separated from the ice reservoir by thermally insulating side walls with a vertical spacing of 1.0 mm. The temperature difference  $\Delta T = T_{IR} - T_{subst}$  determines the effective supersaturation seen by the test crystal. After placing a test crystal we then increase  $\Delta T$  and observe its size and thickness as a function of time, and from this extract growth velocities under various conditions. Our ultimate goal is to understand the crystal growth dynamics as a function of temperature, supersaturation, crystal morphology and history, chemical make-up of the substrate, and the pressure and chemical make-up of the background gas in the experimental chamber.

The means by which we produce these experimental conditions are described in detail in this paper. As experience has shown repeatedly in investigations of ice crystal growth, variations with regard to initial crystal nucleation, growth history, and minute chemical impurities are inevitable in any experimental system. As a result each individual crystal grows somewhat differently, making it difficult to obtain experimental results that describe theoretically perfect ice crystals. A good fraction of this paper is therefore devoted to examining the absolute precision and reproducibility in our measurements under a variety of conditions, and we have also strived to produce quantitative measures of all processes that significantly affect ice growth rates.

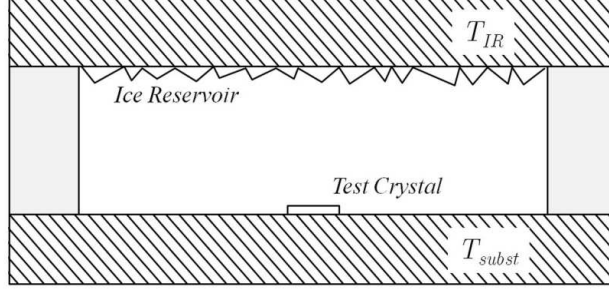


Figure 1: Idealized schematic of our experimental set-up. An ice reservoir at temperature  $T_{IR}$  supplies water vapor for a test crystal resting on a substrate at temperature  $T_{subst}$ . When  $T_{IR} > T_{subst}$ , growth rates are determined by measuring the size and thickness of the test crystal as a function of time.

## 1.1 Basic Growth Modeling

It is instructive to first review the basic growth modeling of ice crystals from water vapor, to define the notation used later. Following the formalism in [1] we write the growth velocity normal to the surface as

$$\begin{aligned} v &= \alpha \frac{c_{sat}}{c_{solid}} \sqrt{\frac{kT}{2\pi m}} \sigma_{surf} \\ &= \alpha v_{kin} \sigma_{surf} \end{aligned} \quad (1)$$

where the latter defines the kinetic velocity  $v_{kin}$ . In this expression  $kT$  is Boltzmann's constant times temperature,  $m$  is the mass of a water molecule,  $c_{solid} = \rho_{ice}/m$  is the molecular number density for ice,  $\sigma_{surf} = (c_{surf} - c_{sat})/c_{sat}$  is the supersaturation just above the growing surface,  $c_{surf}$  is the water vapor number density at the surface,  $c_{sat}(T)$  is the equilibrium number density above a flat ice surface, and  $\alpha \leq 1$  is the condensation coefficient.

For the simple case of a spherical crystal of radius  $R$ , where we neglect any temperature variations from latent heat generation, a straightforward solution of the particle diffusion equation [1] yields the growth velocity

$$\begin{aligned} v &= \frac{\alpha \alpha_{diff}}{\alpha + \alpha_{diff}} v_{kin} \sigma_{\infty} \\ &= \frac{\alpha}{\alpha + \alpha_{diff}} \frac{c_{sat} D \sigma_{\infty}}{c_{solid} R} \end{aligned} \quad (2)$$

where  $\sigma_{\infty}$  is the supersaturation far from the growing crystal,  $D$  is the diffusion constant,  $R$  is the sphere radius, and

$$\begin{aligned} \alpha_{diff} &= \frac{c_{sat} D}{c_{solid} v_{kin} R} = \frac{D}{R} \sqrt{\frac{2\pi m}{kT}} \\ &\approx 0.15 \left( \frac{1 \mu\text{m}}{R} \right) \left( \frac{D}{D_{air}} \right) \end{aligned} \quad (3)$$

where the latter expression is evaluated for the specific case of ice growing at  $T = -15$  C in air. At a pressure of one atmosphere,  $D = D_{air} \approx 2 \times 10^{-5}$  m<sup>2</sup>/sec, while at lower pressures  $D \sim P^{-1}$ .

We note two limiting cases in Equation 2. When  $\alpha \ll \alpha_{diff}$ , then  $\sigma_{surf} \approx \sigma_\infty$  and  $v \approx \alpha v_{kin} \sigma_\infty$ , which describes purely kinetics-limited growth unhindered by particle transport. In the opposite limit,  $\alpha_{diff} \ll \alpha$ , we have  $\alpha(\sigma_{surf})\sigma_{surf} \approx \alpha_{diff}\sigma_\infty$  and  $v \approx \alpha_{diff}v_{kin}\sigma_\infty$ , which describes purely diffusion-limited growth. As we will see below, we have found that that Equation 2 with  $\alpha_{diff}$  as a simple adjustable constant is a useful approximation in many of our experiments.

### 1.1.1 Crystal Heating Effects

An analysis along the same lines as the above can also be used to show the approximate effects of crystal heating generated by solidification in our experiments. At low background pressures, the growth velocity of a hemispherical crystal in thermal contact with the substrate can be written [1]

$$v = \frac{\alpha\alpha_{cond}}{\alpha + \alpha_{cond}}v_{kin}\sigma_\infty \quad (4)$$

with

$$\alpha_{cond} \approx 25G \left( \frac{1 \mu\text{m}}{R} \right) \quad (5)$$

where  $G \approx 1$ . We note that  $\alpha_{cond} \approx \alpha_{diff}$  at a background pressure of  $P \approx 5$  Torr; for higher pressures the effects of crystal heating can be ignored and the growth is limited mainly by particle diffusion and attachment kinetics. Since Equations 2 and 4 have similar functional forms, the overall effects of particle diffusion and heating on the measured crystal growth velocities  $v(\sigma_\infty)$  are also expected to show similar functional forms.

We also note that the temperature difference between the growing top surface of an ice crystal plate and the lower surface (in contact with the substrate) is approximately

$$\begin{aligned} \Delta T &\approx \frac{h v \rho \lambda}{\kappa} \\ &\approx 0.05 \left( \frac{h}{50 \mu\text{m}} \right) \left( \frac{v}{1 \mu\text{m}/\text{sec}} \right) \text{ C} \end{aligned}$$

where  $h$  is the plate thickness,  $v$  is the growth velocity,  $\rho = 917$  kg/m<sup>3</sup> is the density of ice,  $\lambda = 2.8 \times 10^6$  J/kg is the latent heat of solidification from water vapor, and  $\kappa = 2.3$  Wm<sup>-1</sup>K<sup>-1</sup> is the thermal conductivity of ice. In an absolute sense, this difference is also expected to be negligible in our experiments.

## 2 A Series of Ice Growth Chambers

A significant challenge in obtaining accurate ice crystal growth measurements is the production of high-quality test crystals in a well controlled environment. Ideally these crystals should be clean (free from chemical impurities on the ice surface), small (no larger than 50  $\mu\text{m}$ ), free from significant dislocations, isolated at a convenient location on a substrate, and with a well-defined crystal orientation relative to the substrate surface. To accomplish this we have chosen to create free-falling crystals in a large outer chamber and then transport and select crystals in a second, inner chamber. Within the inner chamber, crystals are further placed within a smaller sub-chamber, in which the

supersaturation and temperature are carefully controlled. This strategy separates various experimental functions - nucleating crystals, selecting crystals, and measuring growth rates - into different physical regions, so each function can be better optimized and controlled. We now describe this series of growth chambers in more detail. A number of features of this new apparatus have been adapted and improved from previous versions described in [2] and [3]. A review of earlier related experimental work is given in [1, 4, 5].

## 2.1 The Outer Chamber

Ice crystals are initially created in air within a convection chamber shown schematically in Figure 2, measuring 90 cm in height and 50x50 cm in width and depth (inside dimensions). A programmable chiller cools the copper walls of the chamber by circulating methanol through soldered cooling pipes. Once the system is stable, the chiller can maintain the interior temperature of the chamber down to -35 C with an accuracy of about 0.1 C.

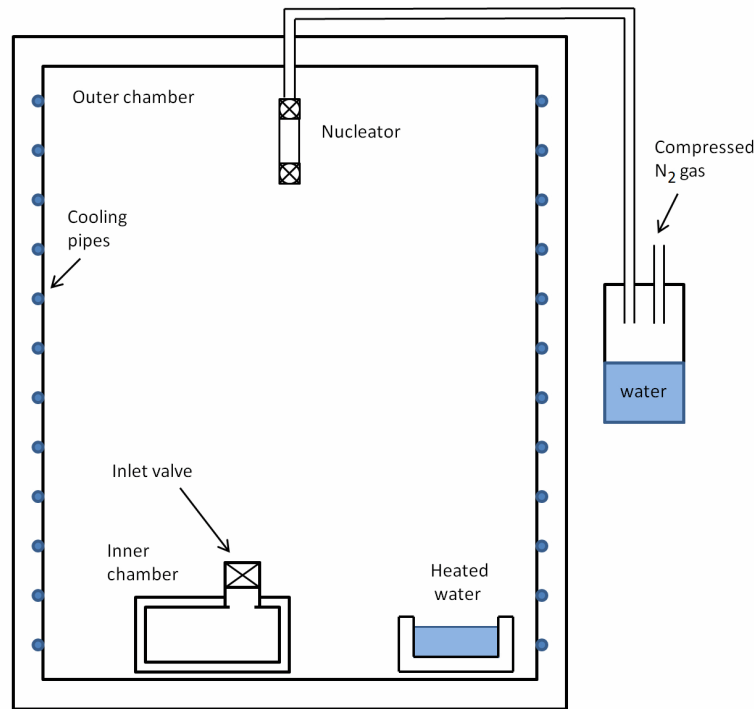


Figure 2: A schematic view (not all parts to scale) of the outer and inner ice crystal growth chambers, as described in the text. Ice crystals are nucleated every ten seconds near the top of the outer chamber, after which they grow in the supersaturated air for several minutes until they become heavy enough to fall to the bottom of the chamber. When desired, an inlet valve is opened to admit crystals into the inner chamber, where their growth rates are measured under controlled conditions.

An insulated reservoir containing heated water located on the bottom of the outer chamber in-

roduces water vapor into the chamber via continuous evaporation. The chamber contains ordinary laboratory air at a pressure of one atmosphere, so convection transports and mixes the water vapor into the air, resulting in a steady-state water vapor supersaturation within the chamber. We have found that the temperature and supersaturation are surprisingly uniform within the chamber [6], indicating efficient mixing by convection. The spatial profile and temporal variability of supersaturation within the chamber are difficult to determine accurately, although these both likely increase monotonically with water temperature [6]. Since the function of the outer chamber is mainly to produce candidate ice crystals, it is not necessary to know the environmental conditions in this region with high accuracy. We typically heat the water to approximately 25 C, and we typically operate with a central temperature of approximately -12.5 C when the goal is to produce thin hexagonal plate crystals.

A pulse of rapidly expanding gas is used to nucleate the growth of ice crystals near the top of the outer chamber [7, 6]. The nucleator is made from a 5-cm-long pipe, 2 cm in diameter, with solenoid-actuated valves on both ends, connected to a source of compressed gas that has been saturated with water vapor from a room-temperature water reservoir, as shown in Figure 2. The first valve is opened for about five seconds to admit compressed gas into the pipe, and then this valve is closed. The second valve is then opened to discharge the compressed gas into the growth chamber. The rapid expansion cools the saturated gas inside the pipe to nucleate small ice crystals [7, 6]. The presence of these faceted crystals is easily verified by observing the sparkle from a bright flashlight shining into the chamber. We typically use nitrogen gas at 20 psi in the nucleator, although argon, helium, and other gases work as well. The nucleator valves are cycled every ten seconds, thus yielding a steady-state of small crystals growing and falling inside the outer chamber.

We estimate that under typical conditions roughly  $10^7 - 10^8$  ice crystals are present in the chamber at any given time, and each grows for about three minutes before gravity causes it to fall to the chamber bottom. The typical size of an ice crystal plate when it reaches the chamber floor is a few microns thick and ~20 microns in diameter. Because there is a continuous downward flow of ice crystals in the chamber, the system as a whole is somewhat self-cleaning. Chemical impurities and dust particles within the chamber are incorporated into growing crystals, which fall and are thus removed. The overall result is that we have a continuous source of rather pristine, newly formed, ice crystals. When desired, an inlet valve (see Figure 2) is opened to admit a random sample of these crystals into the inner chamber for further experimentation.

When the outer chamber is at -12.5 C, we have found that we can transfer crystals to the inner chamber only when its temperature is below -4 C. At higher temperatures, crystals apparently evaporate before reaching the substrate. To take data at higher temperatures we therefore transfer at -4 C and subsequently raise the temperature of the inner chamber to the desired operating temperature. The latter step must be done slowly at a pressure of one atmosphere, while making sure the ice reservoir is kept in equilibrium with the test crystal while the temperature changes.

## 2.2 The Inner Chamber

Figure 3 shows a schematic view of the inner growth chamber, within which ice crystal growth measurements are performed. Air from the outer chamber is drawn into the inner chamber via the inlet valve (shown in Figure 2), depositing a sample of ice crystals onto the sapphire substrate – a disk 50.8 mm in diameter and 1.0 mm thick, with its optic axis oriented along the disk axis (to reduce birefringent effects). Plate-like crystals typically land on the substrate with one basal face in contact with the surface, thus orienting the ice crystal axis relative to the substrate surface.

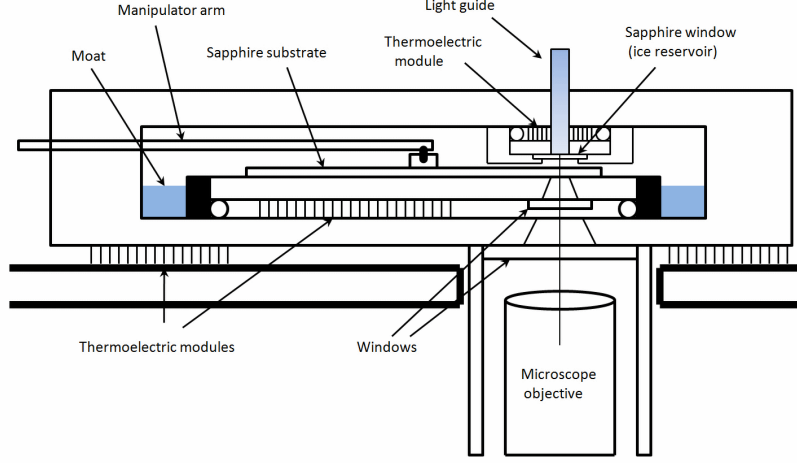


Figure 3: A schematic view (not all parts to scale) of the inner growth chamber, as described in the text. After being admitted through an inlet valve (not shown here; see Figure 2), ice crystals are selected and positioned within an observing region (the experimental sub-chamber described in the text) for subsequent growth measurements.

By rotating this disk about its central axis (using a small silicone o-ring in contact with the outer edge of the disk), and translating it via manipulator arm (shown in Figure 3), it is straightforward to find a suitable ice crystal and position it near the optical axis of the microscope objective for performing subsequent growth measurements. When taking data our goal is usually to position one and only one crystal at the center of the test region, to ensure a well-defined supersaturation during the measurement process.

The inner chamber is a small vacuum chamber constructed to keep the interior as free from vaporous chemical contaminants as is feasible. The chamber body is made from anodized aluminum, as are several interior parts. The temperature-control elements, in particular the greased thermoelectric modules shown in Figure 3 and their associated thermistors and wiring, are all mounted outside the vacuum envelope, separated by silicone o-rings. Other materials inside the chamber include sapphire, coated optical windows, polycarbonate, stainless steel, and a small amount of vacuum-compatible epoxy and vacuum grease (Apiezon N). Several hoses made from polyflow tubing and short lengths of silicone tubing are connected to the inner chamber via stainless steel tubing. The inlet valve is a 1.33-inch stainless steel vacuum butterfly valve retrofit with silicone o-rings. The sapphire substrate is typically cleaned with isopropyl alcohol and rinsed with deionized water between runs, and the water in the moat is removed and replaced between runs as well. The inner chamber is also partially cleaned and baked at 30 C between runs, and the air inside is frequently replaced during a run. With these precautions we believe that chemical influences on our growth measurements are fairly low [8]. Nevertheless, chemical influences cannot be excluded completely, so this remains a potentially significant systematic error in our growth measurements.

The inner chamber base, the chamber lid, and the substrate base are separately temperature

regulated, using thermistor sensors that have an absolute accuracy of better than 0.1 C. Typically the three temperature set-points are identical, producing a nearly isothermal chamber. The temperature of the upper sapphire window (the ice reservoir shown in Figure 3) is then separately temperature regulated to control the supersaturation seen by the test crystal under observation.

Special care was taken in the temperature regulation of the ice reservoir, in order to achieve both high stability and tunability of the supersaturation. We adapted the temperature controller described in [9] for this purpose, adding an additional layer of tunability to achieve very fine set point control. We also read out the temperature controller output voltage  $V_{IR}(T_{IR})$  using a Keithley precision voltmeter that gave microvolt stability over extended periods of time. Calibration and overall accuracy of this temperature control is discussed below.

The inner chamber includes external tubing connections to a vacuum pump, a vacuum gauge, and a gas inlet. The ice moat shown in Figure 3 serves the purpose of keeping the interior of the chamber saturated with water vapor after repeated pump-downs, and at a range of pressures. A diaphragm pump can produce pressures as low as 1 Torr inside the chamber. The microscope objective is at a temperature near room temperature, with two windows and two aluminum thermal baffles separating it from the substrate. A flow of 2 cc/sec of dry nitrogen gas into the partially sealed microscope objective cell is sufficient to prevent condensation on the cold window surface under typical operating conditions.

### 2.3 The Experimental Sub-Chamber

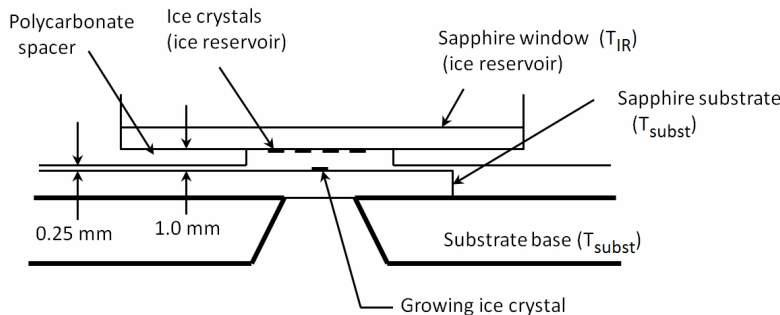


Figure 4: The experimental sub-chamber within the inner ice growth chamber (see Figure 3), as described in the text. This sub-chamber provides an environment with carefully controlled temperature, supersaturation, and background gas pressure, within which we can measure ice crystal growth rates.

Ice growth measurements are performed in the experimental sub-chamber, shown schematically in Figure 4, that is part of the inner growth chamber shown in Figure 3. The top of the sub-chamber is a sapphire window with many ice crystals deposited on its lower surface, and these ice crystals serve as an ice reservoir in our experiments. The sample crystal rests on the sapphire substrate 1.0 mm below the ice reservoir, as shown in Figure 4. A polycarbonate spacer with an 8.1-mm-diameter hole serves as the sub-chamber walls. The sample crystal temperature is equal to  $T_{subst}$  (see Figure

4), and the supersaturation seen by the sample crystal is determined by  $T_{IR} - T_{subst}$ , as described in detail below. The 0.25-mm gap between the substrate and the polycarbonate spacer allows the test crystal to be positioned within the sub-chamber while diminishing the diffusive coupling between the sub-chamber and the surrounding inner chamber.

In practice we tend to operate in one of three pressure regimes: 1) 740 Torr. This pressure is best for selecting crystals, changing system parameters, etc., because the crystals react slowly; 2) 1-2 Torr. At this pressure is it possible to easily add ice to the ice reservoir from the moat; 3) 20 Torr. We have found that this intermediate pressure is near optimal for measuring crystal growth rates. The pressure is high enough to effectively isolate the experimental sub-chamber from the surrounding inner chamber, thus reducing problems from small thermal gradients in the inner chamber. Yet this pressure is low enough that the crystal growth is mainly kinetics limited, thus yielding physically interesting measurements.

## 2.4 The Optical Layout

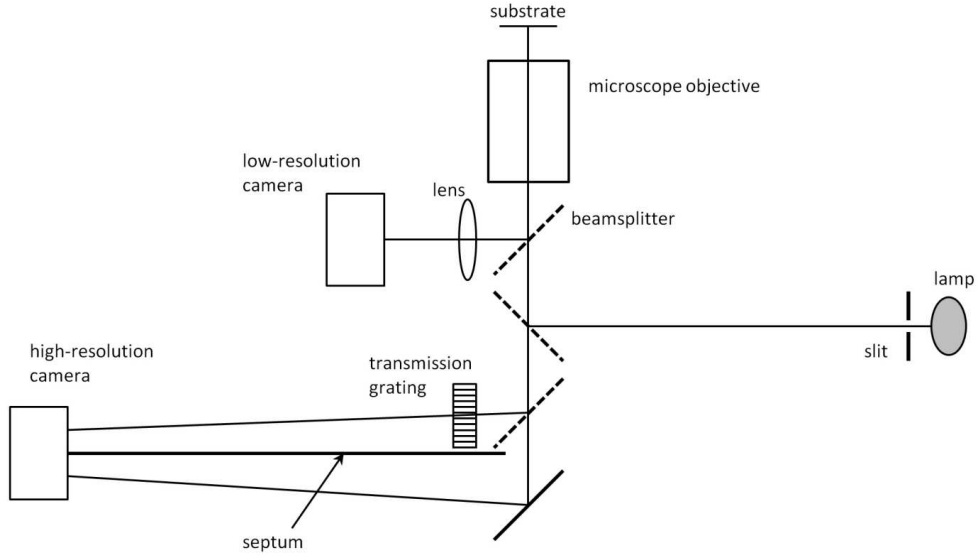


Figure 5: Optical layout (not to scale) for imaging the growing ice crystal on the substrate and measuring its thickness using broad-band interferometry, as described in the text.

The optics are set up to allow simultaneous measurement of 1) the lateral size of the test crystal size via direct imaging, 2) the thickness of the test crystal via broad-band interferometry, and 3) the supersaturation via measurement of  $T_{IR}$ , recording all three measurements in a single video file. Figure 5 shows a schematic diagram of the optics layout.

The microscope objective (10X Mitutoyo Plan Apo) was chosen for its 0.28 numerical aperture, giving a  $1.0 \mu\text{m}$  resolving power, together with its 33.5-mm working distance, which allows ample



Figure 6: Sample display from the high-resolution imaging sensor (see Figure 5), as described in the text.

thermal separation between the room-temperature objective and the substrate, as shown in Figure 3. The crystals are illuminated from above using an external white-light LED that shines through the ice reservoir. The upper beamsplitter is a 10:90 (reflection:transmission) pellicle beamsplitter, and the reflected beam gives a low-magnification image of the test region. This image was mainly used for selecting test crystals and observing any neighboring crystals that grew near the test crystal.

The second beamsplitter is a 50:50 pellicle beamsplitter used to input light for the broad-band interferometer. For the source we chose a halogen bulb with a rather broad coiled filament, using an adjustable mechanical slit to reduce the width of the input source. An image of the bright slit is focused by the objective onto the ice crystal, where some of the light is reflected from the sapphire/ice interface and some is reflected by the ice/air interface. Heating from this light is negligible. The two reflections go back through the objective and two beamsplitters, are reflected by a third beamsplitter (50:50), and pass through a transmission grating (70 lines/mm) to produce a spectrum with interference fringes on the high-magnification imaging sensor. The spacing of the fringes gives the absolute crystal thickness, and small changes in the phase of the fringes allow accurate measurements of growth velocities. Both cameras are Sony Alpha NEX-3 cameras, chosen for their large imaging sensors and good light sensitivity, together with their live HDMI video outputs and HD movie recording modes.

Another portion of the light passes through all three beamsplitters and is steered by mirror M1 onto the high-magnification sensor. A blackened septum prevents overlap of the two incident beams, so the interferometer spectrum is recorded by the top half of the sensor while the direct image appears on the bottom half. Not shown in Figure 5 is a small lens and prism in front of the

high-magnification sensor that projects an image of a television screen onto one corner of the sensor. The television is fed from a camera viewing a precision voltmeter that measures a signal (described below) from which  $T_{IR}$  can be derived.

A sample of the final high-magnification image is shown in Figure 6. The bottom part of the image shows a plate-like ice crystal, hexagonal in shape, here partly obscured by the incident broadband light from the slit. When acquiring data, a shutter periodically blocks the light from the interferometer slit to give a clearer direct image of the crystal. The top part of the image shows the interference spectrum, while the digital voltmeter output appears on the right side of the image. From a video recording of this image we obtain the crystal size and thickness, along with the supersaturation in the experimental sub-chamber, as a function of time. Other experimental parameters are added via the audio channel to the same video file.

## 3 Calibration

### 3.1 Camera Image Scales

An engraved reticle with markings spaced at 0.05 mm was placed directly on the substrate to calibrate the image scale of both cameras. The high-res camera was calibrated in movie mode, since data are acquired in this mode. Note that with the Sony NEX-3 camera the absolute image size in camera mode is different from that in movie mode; different portions of the sensor are used in the two modes. Different movie modes (with different resolutions and aspect ratios) also give different calibrations. Our data were all acquired in VGA movie mode, since the image resolution was more limited by the optics than by the sensor. During a replay of the calibration movie, PaintShopPro was used to do a screen capture and analyze the image. The horizontal distance between the inside edges of the movie frame was found to be

$$L_{horiz} = 400 \pm 1 \text{ } \mu\text{m} \quad (6)$$

The low-res camera was calibrated in a similar fashion. The image circle, defined by the hole in the aluminum substrate support plate directly below the substrate, was found to have a diameter of

$$D = 3.1 \pm 0.1 \text{ mm} \quad (7)$$

### 3.2 Interferometer

The interferometer (IFO) was calibrated by shining red and green lasers through the lamp bulb while the camera was recording in movie mode. When the laser alignment was good, a bright spot appeared at the location of the slit and in the dispersed image. Both lasers were scanned in position to produce a series of spots outlining the slit position. The spots were analyzed using screen captures of the movie replay, and a composite image (IFOcalibration3.jpg) was made. This image shows the various laser spots, lines through the spots, and the superimposed IFO spectrum. A He-Ne ( $\lambda = 633 \text{ nm}$ ) laser and a green laser pointer ( $\lambda = 532 \text{ nm}$ , a frequency-doubled YAG laser) were used.

For data taking, we measure the fringe spacing in the orange part of the spectrum, at  $\lambda_{orange} = 580 \text{ nm}$  as determined from the calibration image. There is a fairly well-defined transition between red and green at this point (see Figure 6), and the fringes are usually fairly clear at this wavelength.

From [6], the reflected intensity can be written

$$I \sim \left[ 1 + \cos \left( \frac{4\pi hn}{\lambda} \right) \right]$$

where  $h$  is the crystal thickness,  $n$  is the index of refraction of ice, and  $\lambda$  is the light wavelength. A phase change of  $2\pi$  corresponds to one IFO cycle (fringe), so

$$\begin{aligned} \Delta \left( \frac{4\pi hn}{\lambda} \right) &= 2\pi \\ \left( \frac{2hn}{\lambda^2} \right) \Delta\lambda &= 1 \\ h &= \frac{\lambda^2}{2n\Delta\lambda} \end{aligned}$$

where  $\Delta\lambda$  is the wavelength difference corresponding to a single fringe.

To complete the calibration we use the measured line positions from IFOcalibration3.jpg. The grating equation tells us that the dispersion of the transmission grating is proportional to  $\Delta\lambda$  (in the small-angle approximation). The distance between the laser lines (101 nm) is measured to be 0.2955 of the full screen width, so the full screen width corresponds to  $\Delta\lambda_{fw} = 342$  nm.

With  $\lambda = \lambda_{orange} = 580$  nm and  $n = 1.31$ , this becomes

$$\begin{aligned} h &= \frac{\lambda^2}{2n\Delta\lambda_{fw}} \left( \frac{\Delta\lambda_{fw}}{\Delta\lambda} \right) \\ &= 0.375 \left( \frac{L_{fw}}{\Delta L_{fringe@orange}} \right) \mu\text{m} \end{aligned} \tag{8}$$

where  $L_{fw}$  is the full-width of the movie screen and  $\Delta L_{fringe}$  is the spacing between adjacent fringes at 580 nm. The largest uncertainty in measuring the thickness of a crystal is from estimating  $\Delta L_{fringe}$  near the orange part of the spectrum, since the fringe spacing varies with wavelength. Achieving an uncertainty of 10 percent or better is straightforward.

The motion of the fringes is used to measure the growth velocity. From the above we see that a single fringe passing by a fixed wavelength  $\lambda$  corresponds to a thickness increase of

$$\begin{aligned} \Delta \left( \frac{4\pi hn}{\lambda} \right) &= 2\pi \\ \Delta h &= \frac{\lambda}{2n} \end{aligned}$$

With a He-Ne laser incident on a crystal this gives  $\Delta h_{HeNe} = 242$  nm. Measuring at  $\lambda = \lambda_{orange} = 580$  nm gives

$$\Delta h_{orange} = 221 \text{ nm} \tag{9}$$

### 3.3 Supersaturation

In the absence of a test crystal, the ice reservoir creates a supersaturation  $\sigma$  immediately above the substrate that is given by

$$\sigma = \frac{\Delta c}{c}$$

$T(^{\circ}\text{C})$	$c_{sat}/c_{solid}$	$v_{kin}(\mu\text{m/s})$	$\eta$	$V_{IR}(\text{volts})$	$dV_{IR}/dT(\text{mV/C})$	$A(\text{V}^{-1})$
-40	$0.13 \times 10^{-6}$	17	0.109			
-30	$0.37 \times 10^{-6}$	49	0.100	1.43	-23.8	4.20
-25	$0.60 \times 10^{-6}$	81	0.096	1.3118	-23.77	4.04
-20	$0.96 \times 10^{-6}$	131	0.092	1.1886	-23.56	3.90
-15	$1.51 \times 10^{-6}$	208	0.088	1.0645	-23.14	3.80
-10	$2.33 \times 10^{-6}$	324	0.085	0.9425	-22.50	3.78
-8	$2.76 \times 10^{-6}$	385	0.084	0.8950	-22.19	3.79
-5	$3.54 \times 10^{-6}$	496	0.082	0.8258	-21.66	3.79
-2	$4.51 \times 10^{-6}$	635	0.080	0.7596	-21.06	3.80
-1	$4.88 \times 10^{-6}$	689	0.079	0.7383	-20.84	3.79

Table 1: Values of various ice properties and calibration quantities as a function of temperature.

$$\begin{aligned}
&\approx \frac{1}{c} \frac{dc}{dT} \Delta T \\
&\approx \eta \Delta T
\end{aligned}$$

where  $\Delta T = T_{IR} - T_{subst}$ ,  $c = c_{sat}(T_{subst})$  is the saturated water vapor pressure of ice, and  $\Delta c = c_{sat}(T_{IR}) - c_{sat}(T_{subst})$ . This is a useful way to write  $\sigma$  because  $\eta$  varies only slowly with temperature. Note that a supersaturation of 1 percent at -15 C corresponds to a temperature difference of  $\Delta T = 0.11$  C.

The temperature difference  $\Delta T$  is obtained from the temperature controller output voltage for the ice reservoir  $V_{IR}(T_{IR})$ . At the beginning of each growth run we determine the  $\sigma = 0$  point by observing when each crystal begins evaporating (see the evaporation tests described below). Once the  $\sigma = 0$  voltage  $V_0$  is known, the temperature difference  $\Delta T = T_{IR} - T_{subst}$  is derived from

$$\begin{aligned}
\Delta V_{IR} &= \left( \frac{dV_{IR}}{dT} \right) \Delta T \\
\Delta T &= \left( \frac{dV_{IR}}{dT} \right)^{-1} \Delta V
\end{aligned}$$

where  $\Delta V = (V_{IR} - V_0)$ , and values for  $(dV_{IR}/dT)$  are determined empirically from a polynomial fit to measurements of  $V_{IR}(T_{IR})$ . We then have the supersaturation

$$\begin{aligned}
\sigma &= \eta \left( \frac{dV_{IR}}{dT} \right)^{-1} \Delta V \\
&= A(T_{subst}) \Delta V
\end{aligned}$$

Table 1 shows values for  $A(T_{subst})$  (accurate to a few percent) as a function of temperature.

### 3.4 Time Delay for Supersaturation Changes

We were mindful of thermal time delays in the ice reservoir, since the thermistor sensing  $T_{IR}$  could not be located in the relevant sapphire window. The propagation time delay between two points along a conductor is approximately

$$\tau \approx \frac{c_p L^2 \rho}{\kappa}$$

where  $c_p$  is the specific heat,  $L$  is a characteristic length,  $\rho$  is the density, and  $\kappa$  is the thermal conductivity. For parts near the ice reservoir,  $\kappa \approx 30$  W/m-K for sapphire (much higher for Aluminum),  $L \approx 3$  mm,  $c_p \approx 1000$  J/kg-K, and  $\rho \approx 2000$  kg/m<sup>3</sup>, giving  $\tau \approx 0.6$  seconds. We examined the time delay by producing sudden jumps in  $T_{IR}$  and observing the subsequent crystal growth behavior. In all cases the growth responded quickly, paralleling the measured  $T_{IR}$ , as expected.

## 4 Initial Measurements

### 4.1 Evaporation Measurements

Once an ice crystal has been transported to the experimental chamber, we typically first determine the saturation point (i. e. where the supersaturation is  $\sigma = 0$ ) by slowly decreasing  $\Delta T$  and observing when the crystal begins to evaporate. This is necessary because the individual measurements of  $T_{IR}$  and  $T_{subst}$  do not have sufficient absolute accuracy to determine the  $\Delta T = 0$  point with the desired precision. Data demonstrating crystal evaporation are shown in Figure 7. The evaporation rates are limited by water vapor diffusion through the surrounding air, as described by an  $\alpha_{diff}$  that depends on air pressure and crystal size (see Equation 3). As expected, we see in Figure 7 that evaporation velocities are substantially higher at lower pressures, reflecting the fact that  $\alpha_{diff}$  is inversely proportional to pressure. The first crystal in Figure 7 had a diameter of 18  $\mu\text{m}$  and a thickness of 3.8  $\mu\text{m}$ , and Equation 3 gave a value of  $\alpha_{diff}$  consistent with that indicated in the data. The second crystal was roughly twice as large, and again the calculated  $\alpha_{diff}$  was consistent with that indicated in the data. As expected, the data suggest  $\alpha_{diff} < \alpha$  in all cases, so the evaporation rates are limited essentially entirely by diffusion.

In practice we do not acquire a great deal of evaporation data for every crystal; instead we reduce  $\Delta T$  only until a crystal shows the first signs of evaporation, as this is typically sufficient to determine the  $\sigma = 0$  point. Shining the light from the interferometer slit on one edge of a crystal and looking for reflection “glints” has proven to be an especially effective method for observing small evaporation changes in real time. In this way we estimate that we can determine the  $\sigma = 0$  point to a temperature uncertainty of approximately  $\Delta T = \pm 0.003$  C in most of our growth measurements at 20 Torr, which corresponds to a supersaturation uncertainty of  $\Delta\sigma \approx \pm 0.03$  percent. Repeated evaporation tests show that temperature drifts in the experimental chamber are typically  $\Delta T \approx \pm 0.003$  C over periods of  $\sim 30$  minutes once the chamber has stabilized.

### 4.2 Droplet Equilibrium Measurements

We were able to test our supersaturation calibration by first increasing  $T_{IR}$  until droplets formed and grew on the substrate, and then adjusting  $T_{IR}$  until the droplets were neither growing nor evaporating. This produced a known supersaturation with  $\sigma = \sigma_{water}$  that we could compare with the value calculated from our calibration. At -15 C, for example, we measured  $\sigma_{water} = 15.3 \pm 1.6\%$ , in agreement with the known value of  $\sigma_{water} = 15.75\%$ . The largest uncertainty came from determining the stability temperature of the droplets.

### 4.3 Basic Growth Measurements

Figure 8 shows a typical measurement of the growth of two ice crystals, both initially produced at -12.5 C in the outer chamber before being transferred into the inner chamber at -15 C. In the

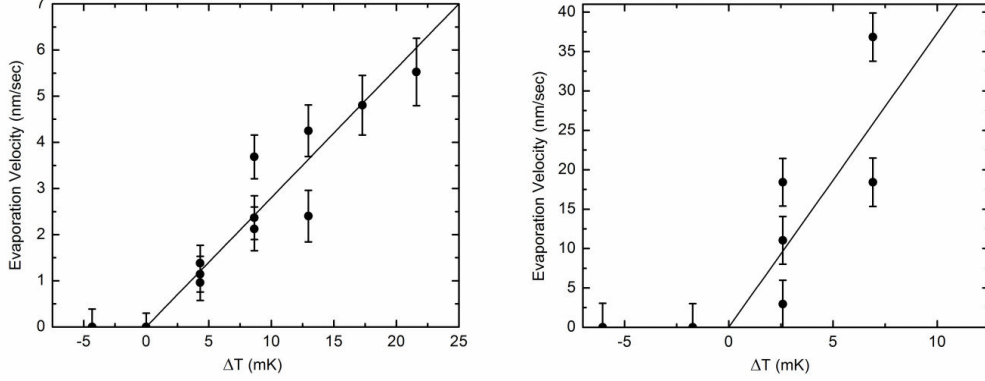


Figure 7: Measurements of evaporation velocities for the basal facets of two ice crystals, as a function of  $\Delta T = T_{subst} - T_{IR}$  as described in the text. The plot on the left shows data taken at a background pressure of 740 Torr, and the plot on the right shows data taken at 20 Torr. Lines show expected velocities for diffusion-limited evaporation with  $\alpha_{diff} = 0.015$  (left) and  $\alpha_{diff} = 0.2$  (right).

experimental sub-chamber, one crystal was grown in air at a background pressure of 20 Torr, while the other was grown at a pressure of 740 Torr. In both cases the supersaturation was slowly increased by increasing  $T_{IR}$  while monitoring the interferometer output to determine the crystal thickness. From this the growth velocity of the basal facet was derived, which in turn was used to extract the condensation coefficient  $\alpha$  as a function of the supersaturation  $\sigma$ .

The basal facets of ice are well described by a nucleation-limited growth model [1], and this is seen in Figure 8 as well. For both crystals we fit the data with curves of the form

$$\alpha(\sigma) = \frac{A \exp(-\sigma_0/\sigma) \alpha_{fit}}{A \exp(-\sigma_0/\sigma) + \alpha_{fit}}$$

where  $\alpha = A \exp(-\sigma_0/\sigma)$  is the intrinsic condensation coefficient of the ice surface and  $\alpha_{fit}$  is a single fit parameter that accounts for particle diffusion to some approximation using Equation 2. The fits used in Figure 8 are  $(A, \sigma_0, \alpha_{fit}) = (1, 2.3, 0.15)$  and  $(1, 2.5, 0.0075)$  for the low-pressure and high-pressure crystals, respectively. Note that  $\alpha_{fit}$  is much lower for the high-pressure crystal, reflecting the fact that the growth is more limited by diffusion in that case. For the low-pressure case, the diffusion term produces only a small improvement in the fit to the data. The data are somewhat insensitive to the choice of  $A$ , so this was fixed at  $A = 1$ , giving the physically reasonable result that the intrinsic  $\alpha \rightarrow 1$  at very high  $\sigma$ .

A significant result from these data, and from numerous similar crystal measurements we have made at -15 C, is that the measured condensation coefficients at high and low pressures are not measurably different other than from the substantial effects of particle diffusion. This contradicts the conclusion made in [10], and we now believe that the reason for this inconsistency is an incorrect interpretation of the data in [11], and we plan to reanalyze these data in a future publication.

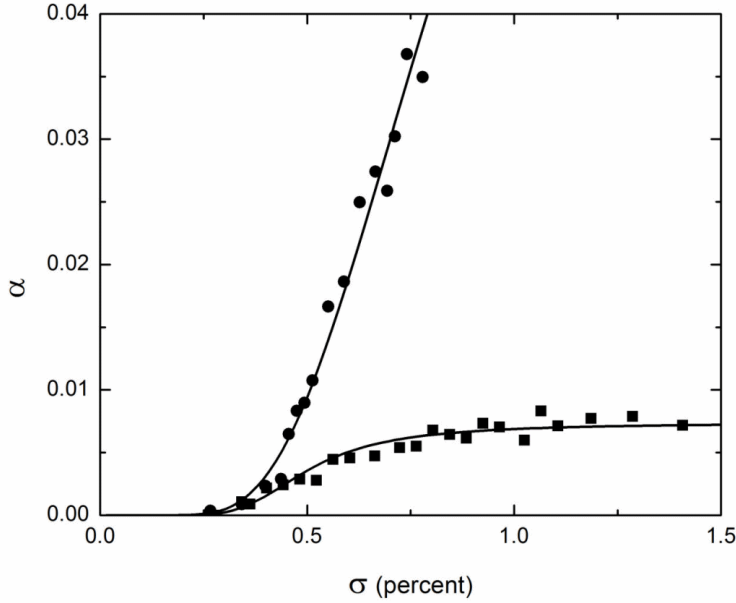


Figure 8: Measurements of the growth of the basal facets of two ice crystals at -15 C, shown as the condensation coefficient  $\alpha$  as a function of supersaturation  $\sigma$ . One crystal (dots) was grown in a background pressure of air at 20 Torr and the other (squares) was grown in a background pressure of 740 Torr. The low-pressure crystal shows mainly kinetics-limited growth, while the growth at high pressure is mainly limited by diffusion when the supersaturation is high.

#### 4.4 Measurements of $\alpha_{diff}$

It is instructive to demonstrate the  $R^{-1}$  dependence of  $\alpha_{diff}$  in a growing crystal, simply as a verification of our understanding of diffusion-limited growth. For this we examined the growth of a large plate-like crystal as it formed above the substrate at 740 Torr at -15 C, atop an ice “pedestal”, essentially one half of a capped column crystal. Figure 9 shows the growth velocity expressed as  $\alpha_{eff} = v(v_{kin}\sigma_{\infty})^{-1}$ , where  $v$  is the measured basal velocity, plotted as a function of the measured plate radius (an average over the hexagonal structure of the plate). For this data  $\sigma_{\infty}$  was held fixed at 0.12 as the crystal grew. The fit line is  $\alpha_{eff} = R_0/R$  with  $R_0 = 0.087 \mu\text{m}$ , and we see that the data show the expected  $R^{-1}$  dependence. This simple model does not take into account the thin edges of the growing plate, nor the geometrical differences between a flat plate and a hemisphere, and these shortcomings likely explain the difference between  $R_0$  and the value found in Equation 3.

A remaining question in this analysis is whether the growth of this crystal is actually diffusion-limited at all points shown in Figure 9. From Equation 2 we see that  $\alpha(\sigma_{surf})\sigma_{surf} = \alpha_{eff}\sigma_{\infty}$ , where  $\alpha_{eff} = \alpha\alpha_{diff}/(\alpha + \alpha_{diff})$  is plotted in Figure 9. Using  $\alpha(\sigma_{surf}) \approx \exp(-0.02/\sigma_{surf})$  (obtained from measurements taken at lower pressures) we estimate that  $\alpha_{diff} \approx \alpha/20$  for the measurements in Figure 9, and thus  $\alpha_{eff} \approx \alpha_{diff}$  and the growth is mainly diffusion limited. Our overall conclusion from this exercise is that the basal growth is well described by diffusion-limited

growth when  $\alpha_{diff} < \alpha$ , in reasonable agreement with expectations.

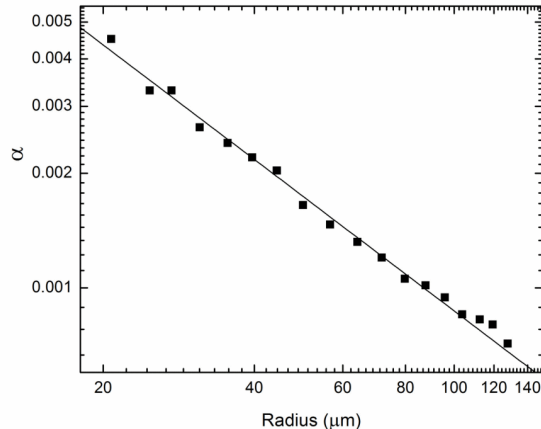


Figure 9: Measurements of the growth rate of the top basal surface of a thin plate crystal at 740 Torr. The data points show  $\alpha_{eff} = v(v_{kin}\sigma_{\infty})^{-1}$  as a function of plate radius, where  $v$  is the measured basal velocity. The fit line is  $\alpha_{eff} = R_0/R$  with  $R_0 = 0.087 \mu\text{m}$ . The data are in good agreement with a simple model for purely diffusion-limited growth, as described in the text.

## 5 Conclusions

In summary, we have constructed an apparatus designed to make precise measurements of ice crystal growth rates from water vapor over a range of environmental conditions. Our particular focus was to produce exceptionally stable and well-defined supersaturations at different temperatures and pressures, in order to measure the intrinsic attachment coefficients for ice growth. Detailed results from experimental measurements with this apparatus will be reported elsewhere.

## References

- [1] Libbrecht, K. G., “The physics of snow crystals,” Rep. Prog. Phys., 68, 855-895 (2005).
- [2] Libbrecht, K. G., “Growth rates of the principal facet of ice between -10C and -40C,” J. Cryst. Growth 247, 530-540 (2003).
- [3] Libbrecht, K. G., “Precision measurements of ice crystal growth rates,” arXiv:cond-mat/0608694 (2006).
- [4] Libbrecht, K. G., “A critical look at ice crystal growth data,” arXiv:cond-mat/0411662 (2004).
- [5] Kobayashi, T., and Kuroda, T., “Snow crystals”, in Morphology of Crystals–Part B, edition I, Sunagawa (Tokyo: Terra Scientific) 645-743 (1987).

- [6] Libbrecht, K. G., and Morrison, H. C., “A convection chamber for measuring ice crystal growth dynamics,” arXiv:0809.4869 (2008).
- [7] Foster, T. C., and Hallett, J., “Ice crystals produced by expansion - experiments and application to aircraft-produced ice,” J. Appl. Meteor. 32, 716-728 (1993).
- [8] Libbrecht, K. G., and Bell, R., “Chemical influences on ice crystal growth from vapor,” arXiv:1101.0127 (2011).
- [9] Libbrecht, K. G., and Libbrecht A. W., “A versatile thermoelectric temperature controller with 10 mK reproducibility and 100 mK absolute accuracy,” Rev. Sci. Instr. 80, 126107 (2009).
- [10] Libbrecht, K. G., “Crystal growth in the presence of surface melting and impurities: An explanation of snow crystal growth morphologies,” arXiv:0810.0689 (2008).
- [11] Libbrecht, K. G., Morrison, H. C., and Faber, B., “Measurements of snow crystal growth dynamics in a free-fall convection chamber,” arXiv:0811.2994 (2008).